

Hierarchical nanostructure of WO₃ nanorods on TiO₂ nanofibers and the enhanced visible light photocatalytic activity for degradation of organic pollutants†

Cite this: *CrystEngComm*, 2013, 15, 5986

Li Zhang,^a Yaogang Li,^a Qinghong Zhang^{*b} and Hongzhi Wang^{*a}

A hierarchically nanostructured TiO₂/WO₃ photocatalyst was synthesized *via* the subsequent hydrothermal treatment of electrospun TiO₂ nanofibers in the presence of tungstic acid. With a uniform WO₃ seed layer providing growth sites, the nucleation on the nanofibers was uniform, thus uniform WO₃ nanorods could be grown. The samples were characterized by scanning electron microscopy (SEM), transmission electron microscopy (TEM), X-ray diffraction (XRD), X-ray photoelectron spectroscopy (XPS), UV-vis diffuse reflectance spectroscopy (DRS), photoluminescence spectra (PL), and Brunauer–Emmett–Teller (BET) method. The results indicated that the WO₃ nanorods with a diameter of about 40 nm and an average length of about 150 nm grew perpendicularly on the TiO₂ nanofibers. The crystallite size and specific surface area of the bare TiO₂ nanofibers were about 30 nm and 46.5 m² g^{−1}. The bare nanofibers are anatase phase with the average diameter of about 350 nm. The TiO₂/WO₃ heterostructures provide more accessible sites for both catalysis and adsorption, and the WO₃ nanorods possess a single crystal structure, which facilitates the migration of the photogenerated electrons. Photocatalytic tests show that the TiO₂/WO₃ heterostructures exhibit a remarkably higher degradation rate of organic pollutants than that of the bare TiO₂ nanofibers under visible light irradiation. The enhanced photocatalytic activity is attributed to the extended absorption in the visible light region and the effective charge separation derived from the coupling effect of TiO₂ and WO₃ nanocomposites.

Received 11th April 2013,
Accepted 15th May 2013

DOI: 10.1039/c3ce40620b

www.rsc.org/crystengcomm

1. Introduction

Photocatalytic oxidation using a titania (TiO₂) based material as the catalyst has attracted substantial attention in recent years, as it is cost-effective, has high catalytic stability and is carried out at room temperature and atmospheric pressure.¹ However, with the band gap of 3.2 eV, anatase phase TiO₂ is only photoactivated under UV light irradiation (of wavelength shorter than 388 nm), which only accounts for 4% of the solar spectrum.² To extend the utilization over the main part (45%) of the visible region in the solar spectrum, several attempts have been made to reduce the band gap of TiO₂. One strategy is preparing modified titania by doping with metallic or non-metallic elements, such as Cu, Mn, Fe, Cr, N, C, and others.³ Though doping with other elements broadened the spectral response range to the visible region, the recombination of electrons and holes may occur on the lattice defects (vacancies,

interstitials and dislocations), which reduce the photocatalytic activity. The noble metals deposition was reported to produce the Schottky barrier and facilitate electron capture.⁴ Therefore, Ag, Ru, and Pt were employed to modify TiO₂ for enhancing UV photocatalytic efficiency and/or visible light activities.⁵ In a very recent work by Dal Santo *et al.*, TiO₂/Au and TiO₂/Pt showed the significantly improved efficiency of more than one order of magnitude in the photocatalytic hydrogen production reaction.⁶ A recent important approach based on the reduction of TiO₂ to induce visible light absorption *via* controlled bandgap engineering is a major breakthrough in visible light utilization; the black TiO₂ nanoparticles obtained through a one-step reduction/crystallization process exhibit a bandgap of only 1.85 eV, which matches well with the visible light absorption.⁷

In recent years, coupling TiO₂ with a narrow band gap semiconductor to broaden the spectral response range and retard photogenerated carrier recombination has attracted considerable attention. Zhu *et al.* fabricated TiO₂/CdS nanocomposites photocatalysts with the bandgap of CdS 2.4 eV, and investigated their visible photocatalytic activity,⁸ however, the photocatalysts have a low stability against photocorrosion

^aState Key Laboratory for Modification of Chemical Fibers and Polymer Materials, Donghua University, Shanghai 201620, P. R. China. E-mail: wanghz@dhu.edu.cn

^bCollege of Materials Science and Engineering, Donghua University, Shanghai 201620, P. R. China. E-mail: zhangqh@dhu.edu.cn

† Electronic supplementary information (ESI) available. See DOI: 10.1039/c3ce40620b

as the sulfur ion is likely to be oxidized to elemental sulfur and precipitated from the solution. Cao *et al.* prepared $\text{TiO}_2/\text{Bi}_4\text{Ti}_3\text{O}_{12}$ heterostructures with the bandgap of 2.5 eV for $\text{Bi}_4\text{Ti}_3\text{O}_{12}$, and demonstrated the photocatalyst exhibited high visible photocatalytic activity. However, the preparation of the ternary semiconductor is relatively complex, with the component being difficult to control.⁹ Obviously, a binary metal oxide semiconductor with narrow bandgap is the ideal candidate for coupling with TiO_2 to obtain the photocatalysts with visible light response. Tungsten oxide (WO_3), a visible-light-responsive photocatalyst with a narrow band gap (2.4–2.8 eV), is harmless and stable in aqueous media over a very wide pH range.¹⁰ WO_3/TiO_2 composite catalysts have been reported to broaden the spectral response range of the visible region and promote the charge transfer.¹¹

The structure and morphology of the photocatalysts have a great influence on their performance. Especially, new hierarchical heterostructures, in which the major one-dimensional (1D) cores and branches consist of different materials, have attracted particular interest. For instance, Xia *et al.* reported that metal nanowires (such as Pt) could be directly grown on the surface of electrospun TiO_2 or ZrO_2 nanofibers using a polyol reduction method to generate nanowire-on-nanofiber hierarchical nanostructures.¹² During the past few years, a series of hierarchical nanostructured photocatalysts with a 1D core consisting of electrospun TiO_2 nanofibers and branches consisting of other materials, such as V_2O_5 , ZnO , BiWO_3 , SnO_2 , NiO , *et al.* have been prepared.¹³ Hierarchically structured nanomaterials with multiscaled organization increase light reflection and absorption inside the materials, leading to an enhanced light utilization rate. Simultaneously, the hierarchically structured nanomaterials also possess an enlarged specific surface area, which effectively increases the attachment and adsorption for contaminants.¹⁴ The nucleation and growth of the secondary structure on the TiO_2 nanofibers enable the TiO_2 core to closely contact with the branches, which were beneficial to the electron transformation. However, to the best of our knowledge, no work has been reported on the use of coupled TiO_2/WO_3 with a hierarchical heterostructures for the photodegradation of organic contaminants.

Herein, we demonstrate a facile route for the synthesis of hierarchically heterostructured TiO_2/WO_3 *via* the hydrothermal treatment of electrospun TiO_2 nanofibers in the presence of tungstic acid. A uniform WO_3 seed layer on the TiO_2 nanofibers provided growth sites, so the nucleation and growth of WO_3 nanorods was uniform. The photocatalytic activity of the hierarchically heterostructured TiO_2/WO_3 was investigated on the degradation of methylene blue (MB) and rhodamine B (RhB) under visible light irradiation. In addition, the photocatalytic mechanism of the hierarchical heterostructured TiO_2/WO_3 was also discussed in detail.

2. Experimental

2.1. Synthesis of TiO_2 nanofibers

The spinning solution for preparing TiO_2 nanofibers contained 4.0 g of tetrabutyl titanate ($\text{Ti}(\text{OC}_4\text{H}_9)_4$, Shanghai Chemical Reagent Company), 4.0 mL of acetic acid (glacial, Shanghai Chemical Reagent Company), 1.4 g of poly(vinyl pyrrolidone) (PVP) ($M_w \approx 1.3 \times 10^6$, Aldrich) and 13 mL of ethanol. The solution was ultrasonicated for 2 h to ensure the homogeneity. A distance of 10 cm and voltage of 12 kV were maintained between the tip of the spinneret and the collector. A grounded wire netting was used as an electrode to collect the nanofibers. The as-spun fibers were calcined at 500 °C for 2 h to burn away the organic compounds and obtain inorganic TiO_2 nanofibers.

2.2. Synthesis of TiO_2/WO_3 hierarchical structures

60 mL of 30 wt% hydrogen peroxide (H_2O_2) was added into a beaker containing 5.0 g of tungstic acid (H_2WO_4 , Shanghai Chemical Reagent Company) powder, and then heated at 95 °C with stirring. Then, 140 mL of H_2O was added into the solution before a transparent sol was obtained. Before hydrothermal growth, a WO_3 seed layer was deposited onto the TiO_2 nanofibers by dipping the TiO_2 nanofibers into the transparent sol for 30 min. The collected precipitates were subsequently annealed at 300 °C for 0.5 h. 40 mL of aqueous solution containing 10 mL of the as-prepared transparent sol and 0.168 g of hexamethylenetetramine (HMT, $\text{C}_6\text{H}_{12}\text{N}_4$) was transferred into a stainless steel Teflon-lined 50 mL autoclave. After the TiO_2 nanofibers were added into the reaction system, the autoclave was sealed and kept at 180 °C for 6 h (T-180-6), 12 h (T-180-12), and 18 h (T-180-18) and at 150 °C for 12 h (T-150-12) in an oven. The obtained products were collected and washed with absolute ethanol and deionized water for five more times and then dried in an oven at 50 °C.

2.3. Sample characterization

The morphologies of the samples were characterized with a field emission scanning electron microscope (FESEM, Hitachi S-4800) operated at an accelerating voltage of 5 kV. TEM images were obtained using a JEM-2100 F TEM (JEOL Tokyo Japan) operating at 200 kV equipped with a LINK probe for energy dispersive X-ray (EDX) spectroscopy analysis. X-Ray diffraction (XRD) was carried out on a Rigaku-D/max 2550 PC (Japan) diffractometer with Cu K α radiation ($\lambda = 1.5406 \text{ \AA}$). X-ray photoelectron spectroscopy (XPS) measurements were carried out with an SECA Lab 220i-XL spectrometer by using an unmonochromated Al K α (1486.6 eV) X-ray source. All the spectra were calibrated to the binding energy of the adventitious C 1s peak at 284.6 eV. The porous properties of samples were investigated using physical adsorption of N_2 at liquid-nitrogen temperature on an automatic volumetric sorption analyzer Autosorb-1 MP (Quantachrom SI, USA). DRS spectra were recorded on a PerkinElmer Lambda 950 instrument, using BaSO_4 as the reference sample, in the range of 200–800 nm. Photoluminescence (PL) was measured at room temperature in a PerkinElmer LS55 luminescence spectrometer with a xenon lamp as the excitation source, and the excited wavelength was 300 nm.

2.4. Photocatalytic tests

In a typical reaction, irradiation was performed with a 500 W xenon lamp and a ZJB 420 filter glass was used to cut off the light with wavelengths less than 420 nm. 0.10 g of photocatalyst was added into a 450 mL Pyrex photoreactor containing 100 mL of 3.8×10^{-5} M MB or RhB (1×10^{-5} M). The concentrations of the solutions were monitored colorimetrically by using a Lambda 35 ultraviolet-visible (UV-vis) absorption spectrophotometer (PerkinElmer, USA).

For comparison, the WO_3 nanoparticles were also prepared *via* hydrothermal treatment of the tungstic acid solution at 180°C for 12 h. The bulk WO_3/TiO_2 powder was prepared by mechanical mixing TiO_2 with WO_3 and calcining at 500°C for 2 h (TiO_2/WO_3 MM).

3. Results and discussion

X-Ray diffraction (XRD) analysis was employed to investigate the evolution of crystal phases during the formation of the hierarchically structured TiO_2/WO_3 nanofibers. Fig. 1a shows the XRD pattern of the bare TiO_2 nanofibers, in which all the diffraction peaks were indexed as anatase TiO_2 (JCPDS 21-1272).¹⁵ After hydrothermal treatment for 6 h, the peaks belonging to monoclinic WO_3 and rutile TiO_2 appeared, as shown in Fig. 1b. Treating anatase TiO_2 nanofibers in an acidic solution, about 63.5 wt% of anatase TiO_2 was changed into rutile TiO_2 according to published work on the weight fraction of rutile in the powder.¹⁶ The weak peaks at 23.15 – 24.35° , which belong to WO_3 , also appeared, while there was no nanorod found on the surface of the TiO_2 nanofibers, as shown in Fig. S1a (ESI†). After hydrothermal treatment for 12 h, the characteristic triple peak at 23.15 – 24.35° became stronger, and the diffraction peaks appearing at 28.8° , 34.2° and 49.9° were indexed as monoclinic WO_3 (JCPDS 43-1035).¹⁷ Both oxides exist in the composite hierarchical nanostructures as separated phases, and no indication of a mixed compound can be observed from the peaks in Fig. 1c. Further increasing

the time for the hydrothermal treatment to 18 h, the intensity of the monoclinic WO_3 peaks became stronger due to the growth of the WO_3 nanorods (Fig. 1d). However, all the anatase TiO_2 changed into rutile TiO_2 , which was disadvantageous to the photocatalysis. Fig. 1e shows the XRD pattern of the WO_3 nanoparticles prepared by hydrothermal treatment of the tungstic acid solution at 180°C for 12 h, in which all the diffraction peaks were indexed as monoclinic WO_3 . The XRD pattern of the samples displayed a significant degree of preferred orientation as could be deduced from the relative intensities of the characteristic triple peak at 23.15 – 24.35° . The relative intensity of $I_{002}/I_{020}/I_{200}$ for the sample T-180-12, T-180-18, and the WO_3 nanoparticles are 77/86/100, 89/100/95 and 93/89/100, respectively, those in samples T-180-12 and T-180-18 are somewhat different from the 100/97/99 reported as JCPDS 43-1035. The increasing relative intensity of the (0 2 0) peak of the sample T-180-18 indicates that when increasing the hydrothermal time to 18 h, the oriented growth of the nanorods have a preferential direction growth along the *b* axis.

Fig. 2a shows a typical SEM image of the as-synthesized hierarchically structured TiO_2/WO_3 nanofibers of T-180-12,

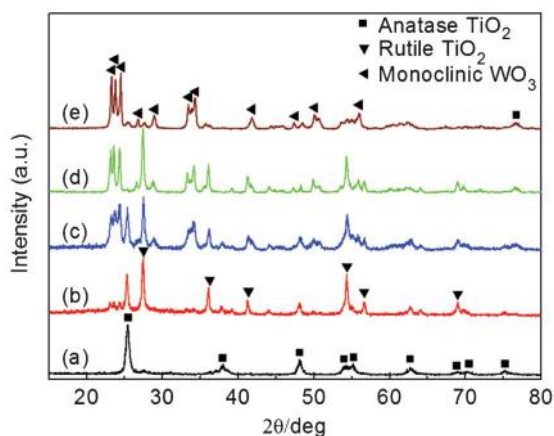


Fig. 1 XRD patterns of the bare TiO_2 nanofibers (a), the samples of T-180-6 (b), T-180-12 (c), and T-180-18 (d), and the WO_3 nanoparticles (e).

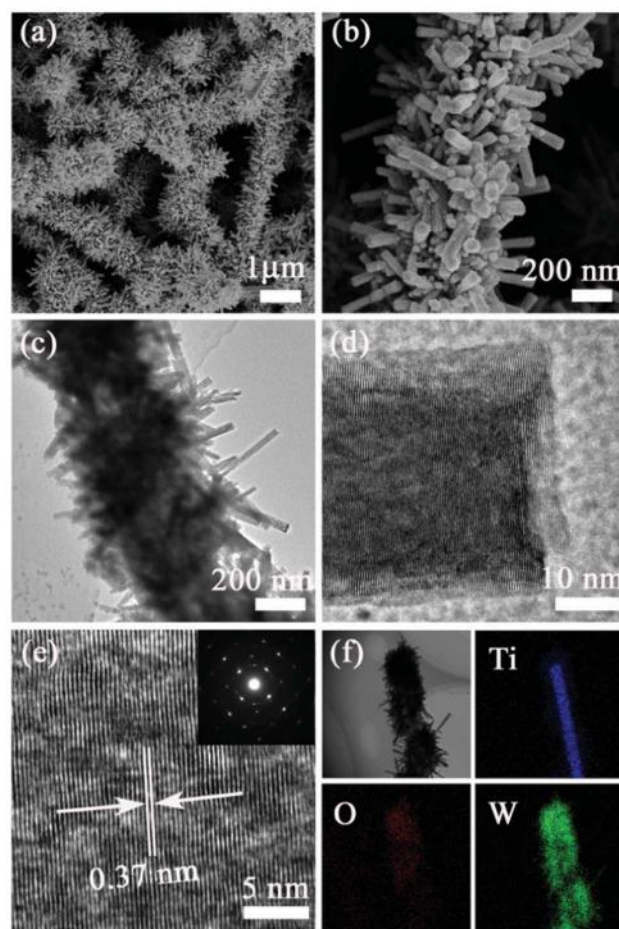


Fig. 2 SEM images of the sample of T-180-12 (a) and a single fiber (b) in (a). TEM images of a single TiO_2/WO_3 nanofiber (c) and WO_3 nanorod (d) in the sample of T-180-12. HRTEM image of the WO_3 nanorod (e); the inset is the corresponding SAED pattern. EDX images of a single TiO_2/WO_3 nanofiber (f).

where the WO_3 nanorods were uniformly distributed across the entire surface of each fiber forming a network of relief features on the rough surface of each TiO_2 nanofiber. As shown in Fig. 2b, it could be observed that the WO_3 nanorods were in fact very fine rods with an average diameter of *ca.* 40 nm and an average length of *ca.* 150 nm. Further information about T-180-12 was obtained from the TEM images (Fig. 2c). It is confirmed that the nanofibers have diameters of about 200 nm, which agrees well with that revealed by the SEM images. Close observation on the WO_3 nanorod (Fig. 2d) reveals that the WO_3 nanorods are well crystallized with a diameter of *ca.* 40 nm. The lattice fringes on the nanorod indicate that WO_3 processes a single crystal structure, which may facilitate the migration of the electrons. Fig. 2e shows a high-resolution TEM (HRTEM) image recorded from the edge of one WO_3 nanorod. The fringe spacing of 0.37 nm agrees well with the spacing of the (0 0 2) lattice planes of WO_3 .¹⁸ The diffraction spots of the corresponding selected area electron diffraction (SAED) pattern can be indexed as the (2 0 0) and (0 0 2) reflections (inset in Fig. 2e), which demonstrates that the WO_3 nanorods are structurally uniform and could be described as single crystals with [0 0 2] growth direction.¹⁹ A dark-field TEM image with the corresponding EDX elemental mapping of the same nanofiber region indicates spatial distribution of O (red), W (green), and Ti (blue), which further confirms that the WO_3 nanorods have grown on the TiO_2 nanofibers (Fig. 2f).

Fig. S1a (ESI†) shows the SEM image of the sample T-180-6, where the product was WO_3 nanoparticles deposited on the TiO_2 nanofibers. However, after hydrothermal treatment of the TiO_2 nanofibers for 18 h, the WO_3 nanorods were formed on the surface of the TiO_2 nanofibers, as shown in Fig. S1b, ESI.† In a shortened duration, the temperature and pressure in the autoclave are not appropriate for the WO_3 to grow into nanorods. Fig. S1c, ESI.† shows the SEM image of the sample T-150-12, where WO_3 nanoparticles but not nanorods were found to be piled up on the TiO_2 nanofibers, and the possible reason is that the nucleation rate is greater than the growth rate in the autoclave at 150 °C; too many WO_3 nuclei formed but did not further grow into nanorods.

Fig. 3 shows the high-resolution Ti 2p, O 1s, and W 4f XPS spectra of the sample of T-180-12. As shown in Fig. 3a, there are two peaks in the Ti 2p region. The peak located at 464.2 eV corresponds to the Ti 2p_{1/2} and another one located at 458.5 eV is assigned to Ti 2p_{3/2}.²⁰ The splitting between Ti 2p_{1/2} and Ti 2p_{3/2} is 5.7 eV, indicating a normal state of Ti^{4+} in the as-prepared TiO_2/WO_3 heterostructures. In Fig. 3b, the W 4f_{7/2} peak is located at 35.4 eV and the W 4f_{5/2} peak is found at 37.5 eV. The splitting of the 4f doublet of W is 2.1 eV, indicating that the valence state of W is +6.²¹ The absence of W^{5+} , W^{4+} , and W^0 in the sample indicates that after hydrothermal treatment for 12 h the nanorods grown on the TiO_2 nanofibers were WO_3 , not other intermediates, such as WO_2 , $\text{W}_{20}\text{O}_{58}$, $\text{W}_{18}\text{O}_{49}$ or hydrogen bronzes H_xWO_3 . Fig. 3c presents the O 1s photoelectron peaks. The wide and asymmetric peak of the O 1s spectrum can be fitted with three Gaussian functions at 530.0, 530.9, and 532.3 eV, indicating the existence of crystal

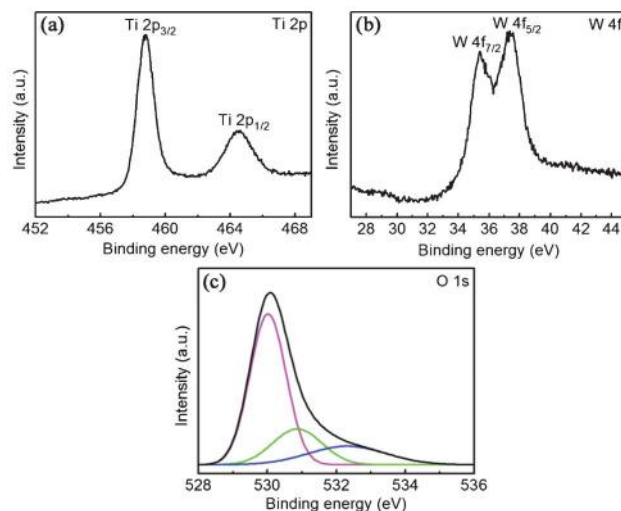


Fig. 3 X-ray photoelectron spectroscopy of (a) Ti 2p, (b) W 4f and (c) O 1s of the sample of T-180-12.

lattice oxygen ($\text{O}_{\text{Ti-O}}$ or $\text{O}_{\text{W-O}}$), hydroxyl groups (O_{OH}), and absorbed water.

The UV-vis DRS of the bare TiO_2 nanofibers and the sample T-180-12 are shown in Fig. 4. It can be seen that the absorption edge for the sample of T-180-12 is shifted toward the visible region compared to that of the bare TiO_2 nanofibers. The main absorption edge for the bare TiO_2 nanofibers is estimated to be 389 nm, which can be attributed to the intrinsic absorption band derived from the band gap transition.²² Compared with the bare TiO_2 nanofibers, the hierarchically structured TiO_2/WO_3 nanofibers present two absorption edges located at *ca.* 417 and 460 nm, which are attributed to the intrinsic absorption band derived from the bandgap transition of TiO_2 and WO_3 , respectively. The WO_3 band gap energy was calculated to be 2.7 eV using the relation $E_g = 1240/\lambda$, where λ is the onset absorption wavelength (460 nm).²³ After coupling

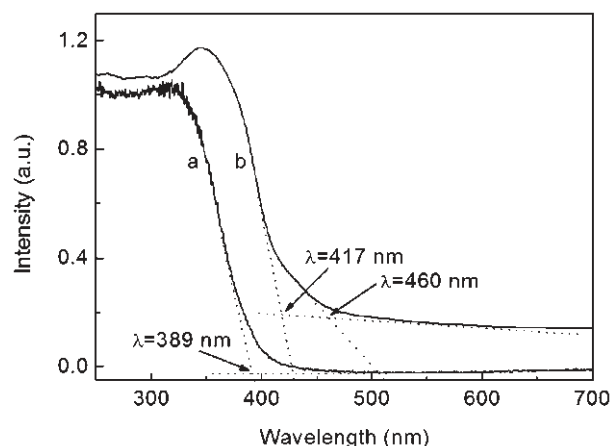


Fig. 4 UV-vis diffuse reflectance spectra of the bare TiO_2 nanofibers (a) and the sample of T-180-12 (b).

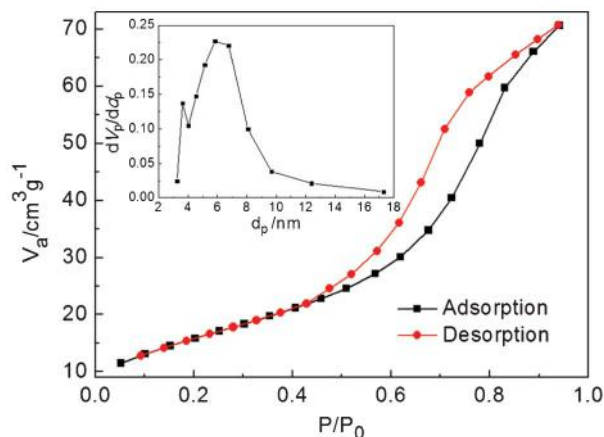
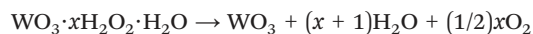
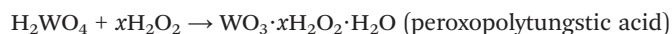


Fig. 5 N_2 adsorption-desorption isotherms and pore size distribution (inset) of the sample of T-180-12.

with the narrow band gap of WO_3 , the hierarchically structured TiO_2/WO_3 composite increased the utilization of visible light, which could accordingly lead to a higher visible photocatalytic activity.

N_2 adsorption-desorption isotherms and calculated pore size distribution curves of the hierarchically structured TiO_2/WO_3 nanofibers of the sample of T-180-12 are shown in Fig. 5. According to the IUPAC nomenclature, the hierarchically structured TiO_2/WO_3 nanofibers exhibit a type IV isotherm, with type H1 hysteresis loops for the relative pressure P/P_0 in the range 0.5–1.0.²⁴ The pore size distribution (Fig. 5, inset) curves are derived by the Barret-Joyner-Halenda (BJH) method, which reveal a bimodal and narrow pore size distribution centered at about 6.5 nm. In addition, a Brunauer-Emmett-Teller (BET) analysis shows that the surface areas of the hierarchically structured TiO_2/WO_3 nanofibers are $25.5 \text{ m}^2 \text{ g}^{-1}$, smaller than those of the bare TiO_2 nanofibers ($46.5 \text{ m}^2 \text{ g}^{-1}$). The decreasing surface areas of the sample T-180-12 are due to the WO_3 nanorods having a larger crystallite size and density than that of TiO_2 . It is well known that large surface areas of catalysts are beneficial to adsorb pollutants in aqueous solution and increase the contact areas between the catalysts and the pollutants during the photocatalysis, however, the surface area of $25.5 \text{ m}^2 \text{ g}^{-1}$ is still high enough for the photocatalysis.

The growth mechanism of the uniform WO_3 nanorods on the TiO_2 nanofibers can be explained according to the following reactions:²⁵



Firstly, H_2WO_4 powder was dissolved *via* the addition of H_2O_2 , and peroxopolytungstic acid (PTA) was formed.²⁵ WO_3 crystal nuclei were obtained and then nucleated to form primary particles from the PTA precursor under hydrothermal

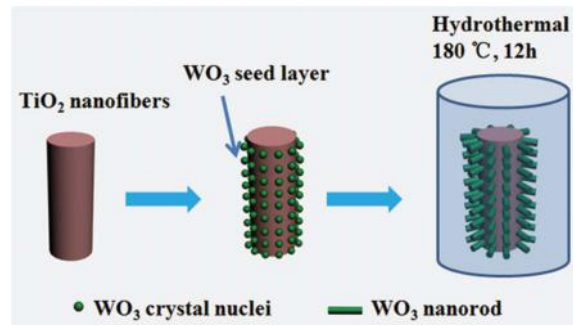


Fig. 6 Schematic illustration showing the formation of the hierarchically structured TiO_2/WO_3 nanofibers.

treatment at 180°C . The seed layer deposited on the TiO_2 nanofibers provided growth sites for the WO_3 nanorods. As shown in Fig. 6 of the schematic illustration of the formation mechanism, with a uniform WO_3 seed layer providing growth sites, the nucleation on the nanofibers was uniform, thus uniform WO_3 nanorods could be grown. Fig. S2 (ESI†) shows the SEM images of the bare TiO_2 nanofibers (a), the TiO_2 nanofibers with WO_3 seed layer deposited onto them (b), and the high magnification of b (c). It can be observed that the surface of the bare nanofibers was smooth, while the surface of the TiO_2 nanofibers with a WO_3 seed layer deposited onto them was not as smooth as the bare nanofibers. As shown in Fig. S2c, ESI†, the WO_3 seeds with the size of 10–20 nm were uniformly deposited onto the TiO_2 nanofibers, which guarantees the nucleation of WO_3 on the nanofiber was uniform. The nucleation and crystal growth of WO_3 were carried out in the autoclave during the hydrothermal treatment. HMT molecules adsorbed on the surfaces of the WO_3 nanocrystals served as surface-anchored molecules, and drove the oriented attachment growth of these nanocrystals during the hydrothermal treatment. In the presence of HMT in the solution, the WO_3 primary particles aggregated along the $[0\ 0\ 2]$ direction of the hexagonal WO_3 unit cell *via* oriented attachment, because HMT molecules preferentially adsorbed on the faces parallel to the *c*-axis of the WO_3 nanocrystal, and thus 1D single crystal structured nanorods were formed. For comparison, in the absence of HMT, there were no WO_3 nanorods formed due to the random aggregation of WO_3 primary particles, as shown in Fig. S3a (ESI†). Similarly, in the absence of the WO_3 seed layer on the TiO_2 nanofibers to provide growth sites, the WO_3 nanorods also can't be grown on the nanofibers (Fig. S3b, ESI†). By means of the oriented attachment growth of surface-stabilized nanocrystals, hydrothermal products with perfect hierarchical nanofiber-nanorod morphology were finally obtained.

Fig. 7a shows the photodegradation rate of different photocatalysts under visible light irradiation, where C was the absorption of MB at the wavelength of 664 nm and C_0 was the absorption after the adsorption equilibrium on the samples prior to irradiation. A blank test (MB without any catalyst) under visible light exhibited little photolysis. The

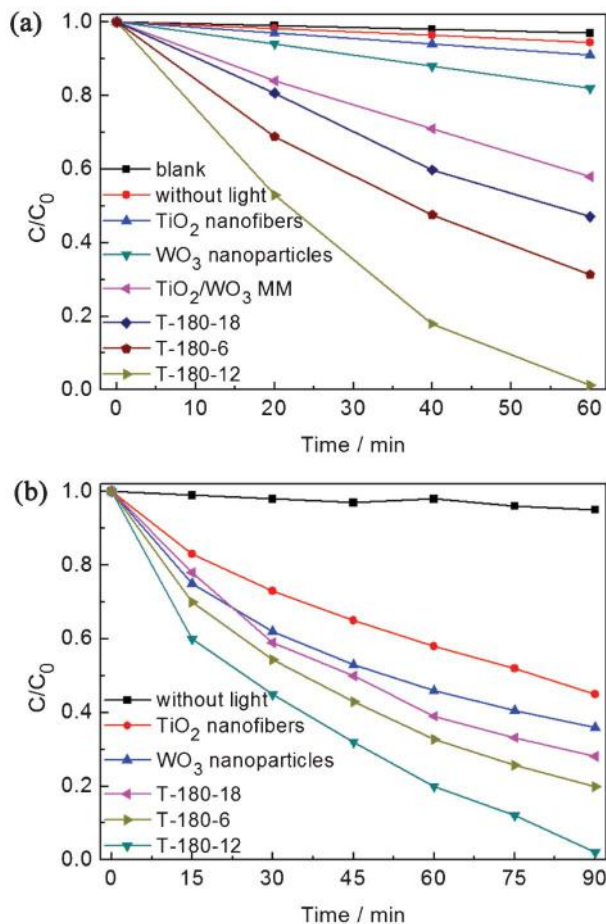


Fig. 7 (a) The photocatalytic degradation of MB over TiO₂ nanofibers, WO₃ nanoparticles, TiO₂/WO₃ prepared by mechanically mixing TiO₂ with WO₃ (TiO₂/WO₃ MM), and the samples of T-180-6, T-180-12, and T-180-18. (b) The photocatalytic degradation of RhB over TiO₂ nanofibers, WO₃ nanoparticles, and the samples of T-180-6, T-180-12, and T-180-18.

decrease of MB concentration with the sample of T-180-12 in the dark for 60 min was similar to that of the blank test. The photodegradation efficiency of MB reaches nearly 100% after 60 min under visible light irradiation with the sample of T-180-12, which was much higher than that of the bare TiO₂ nanofibers, WO₃ nanoparticles, and TiO₂/WO₃ powders prepared by mechanical mixing of TiO₂ with WO₃ and calcining at 500 °C (TiO₂/WO₃ MM). The photocatalytic activities of samples were further evaluated for the photodegradation of RhB under visible light irradiation. Fig. 7b displays the time profiles of C/C_0 over TiO₂ nanofibers, WO₃ nanoparticles and hierarchically structured TiO₂/WO₃ nanofibers under visible light irradiation. After 20 min irradiation with visible light, about 50% of RhB was degraded in the presence of T-180-12, while approximately 50 and 80 min were required to reach the same level of degradation with WO₃ nanoparticles and TiO₂ nanofibers, respectively. This confirmed the superiority of the hierarchically structured TiO₂/WO₃ nanofibers over WO₃ nanoparticles and TiO₂ nanofibers. Moreover, the photoactivity of T-180-12 is higher than that of T-180-6, as the nanorods

were not formed on the surface of TiO₂ nanofibers. The sample of T-180-18 had the hierarchical structure, but the TiO₂ nanofibers were rutile after the hydrothermal treatment, so the photoactivity of T-180-18 was even lower than that of T-180-6.

The efficient photodecomposition of organic pollutants on the surface of the hierarchically structured TiO₂/WO₃ nanofibers under visible light irradiation is determined by several factors. Firstly, as the 3D hierarchically heterostructured photocatalysts provide more accessible sites for both catalysis and adsorption, more organic pollutants are adsorbed and subsequently photocatalytically degraded. Secondly, TiO₂ nanofibers and WO₃ nanorods are in close contact with each other, facilitating the photogenerated electrons or holes transfer from one semiconductor to another. Unlike the transport of electrons in a polycrystalline structure, which is hindered due to grain boundaries, the single crystal structured WO₃ nanorods make the transport of electrons to the surface unobstructed, which facilitates the separation of the photo-generated carriers and improves the photocatalytic reaction rate. Last but not least, from the energy band structure diagram of the TiO₂/WO₃ hierarchical heterostructure in Fig. 8, it can be found that photogenerated electron transfer occurred from the conduction band (CB) of TiO₂ to the CB of WO₃ and photogenerated hole transfer could take place from the valence band (VB) of WO₃ to the VB of TiO₂. The transfer of photogenerated carriers was accompanied by consecutive W⁶⁺ reduction into W⁵⁺ by the capture of photogenerated electrons at trapping sites in WO₃.²⁶ At the same time, W⁵⁺ ions on the surface of WO₃ nanorods were reoxidized into W⁶⁺ by oxygen that was subsequently reduced into O₂^{•−}. The recycling of the electron leads to an increase in the lifetime of the photo-generated pairs and as a consequence to a promotion of the photonic efficiency for the degradation of organic pollutants. Holes were then captured by surface hydroxyl groups (OH[−]) on the photocatalyst surface and yielded hydroxyl radicals (OH[•]).²⁷ The formed superoxide anions (O₂^{•−}) may either attack the organic molecules of MB or RhB directly or generate

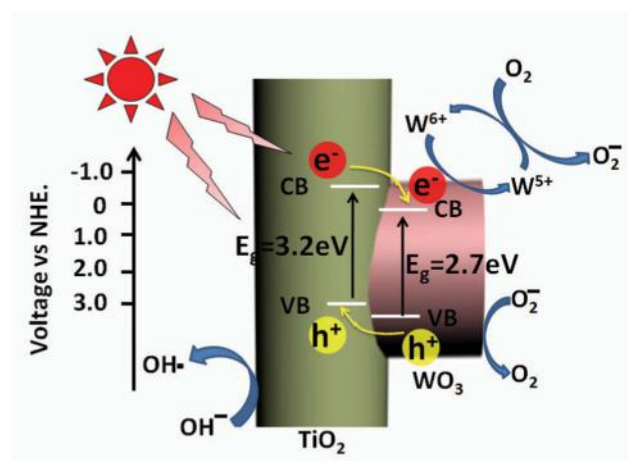


Fig. 8 Schematic diagram showing the energy band structure and electron-hole pair separation in the hierarchically structured TiO₂/WO₃ nanofibers.

hydroxyl radicals (OH^\bullet) by reacting with photogenerated electrons and hydrogen ions (H^+).²⁸ Finally, the strong oxidizing agents, hydroxyl radicals (OH^\bullet), degraded the organic dyes of MB or RhB. Furthermore, the better separation of photogenerated electrons and holes in the hierarchically structured TiO_2/WO_3 nanofibers was verified by PL emission spectra, as the PL emission spectra are related to the transfer behavior of the photogenerated carriers.²⁹ Fig. 9 shows the PL spectra of the bare TiO_2 nanofibers, the hierarchically structured TiO_2/WO_3 nanofibers of the sample T-180-12 and the pure WO_3 nanoparticles. It can be seen that all the three samples exhibited obvious PL signals upon irradiation with 300 nm light. Coupling WO_3 nanorods had a great effect on the PL intensity of the TiO_2 nanofibers, and the PL intensity decreased dramatically when the WO_3 nanorods grew on the surface of TiO_2 nanofibers. For the bare TiO_2 nanofibers, we assign high-energy peaks at 406 and 420 nm to surface recombination of the anatase TiO_2 , while the lower-energy peaks/shoulders at 443, 450, 464 and 485 nm are induced by the presence of oxygen vacancies in the TiO_2 nanofibers (Fig. 9a).³⁰ After coupling with WO_3 nanorods, the surface recombination for the electrons and holes is inhibited, so the decreased PL intensity is especially evident for the bands at 400–430 nm (Fig. 9b). While the bands at lower energy are less affected, since coupling with WO_3 nanorods could not reduce the influence of oxygen vacancies in the TiO_2 nanofibers. As shown in Fig. 9c, the as-prepared WO_3 nanoparticles exhibit five luminescence emissions at 416 nm, 450 nm, 467 nm, 481 nm and 491 nm. The two minor emissions at 450 nm and 481 nm are attributed to surface defects,^{10,31} while the strong emission peak at 467 nm is ascribed to the recombination of electron–hole pairs excited on the surface of WO_3 nanoparticles.³² Since the emission of WO_3 is weaker than that of TiO_2 , the PL emission peak resulting from the presence of the oxygen vacancies in the TiO_2 nanofibers covers up the decrease of the PL emission induced by coupling with WO_3 . On the basis of these findings, it was concluded that coupling with

WO_3 resulted in the formation of heterojunctions between the TiO_2 nanofibers and the WO_3 nanorods. The potential difference between TiO_2 and WO_3 allowed photoelectrons to easily migrate from the TiO_2 surfaces to the WO_3 conduction band. This resulted in a decrease in the radiation recombination of photogenerated electrons on the TiO_2 nanofibers surfaces. Thus, the decreased PL intensity of the hierarchically structured TiO_2/WO_3 nanofibers indicates a high quantum efficiency and high photocatalytic activity.

4. Conclusion

A novel composite photocatalyst of hierarchically structured TiO_2/WO_3 nanofibers was developed by hydrothermal treatment of TiO_2 nanofibers fabricated by an electrospinning method. The WO_3 seed layer on the TiO_2 nanofibers provides growth sites, facilitating the nucleation and growth in the solution, thus TiO_2 nanofibers and WO_3 nanorods were closely combined together. These heterostructures demonstrated enhanced visible light absorption and increased photocatalytic degradation of organic pollutants. Under visible light irradiation, the migration of electron–hole pairs between TiO_2 and WO_3 increased the lifetime of the charge carriers, beneficial for improving the photoactivity. In addition, TiO_2/WO_3 heterostructures have large surface areas and light utilization, meanwhile single crystal WO_3 nanorods make the migration of electrons to the surface unobstructed, which facilitates the separation of the photogenerated carriers and improves the photocatalytic reaction rate. Furthermore, the developed approach to growing uniform WO_3 nanorods onto TiO_2 nanofibers may also be extended for tailoring the size, composition, and surface properties of other three-dimensional porous nanostructured materials with a high surface area for various applications, including but not limited to catalysis, sensing, environmental remediation, and biomedicine.

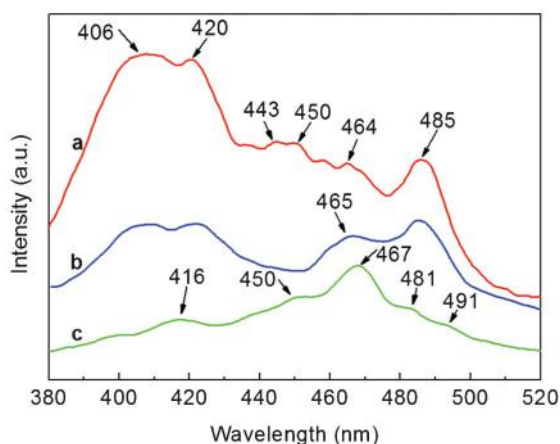


Fig. 9 PL spectra of the bare TiO_2 nanofibers (a), the hierarchically structured TiO_2/WO_3 nanofibers of the sample T-180-12 (b), and the pure WO_3 nanoparticles (c).

Acknowledgements

The authors gratefully acknowledge the financial support by Natural Science Foundation of China (No. 51072034), Innovation Program of Shanghai Municipal Education Commission, the Cultivation Fund of the Key Scientific and Technical Innovation Project (No. 708039), the Program for Professor of Special Appointment (Eastern Scholar) at Shanghai Institutions of Higher Learning, and the Program of Introducing Talents of Discipline to Universities (No. 111-2-04).

References

- (a) A. Fujishima and X. T. Zhang, *C. R. Chim.*, 2006, **9**, 750;
(b) J. H. Mo, Y. P. Zhang, Q. J. Xu, J. J. Lamson and R. Y. Zhao, *Atmos. Environ.*, 2009, **43**, 2229.

- 2 M. R. Hoffmann, S. T. Martin, W. Y. Choi and D. W. Bahnemann, *Chem. Rev.*, 1995, **95**, 69.
- 3 (a) R. Asahi, T. Morikawa, T. Ohwaki, K. Aoki and T. Taga, *Science*, 2001, **293**, 269; (b) H. Y. Xie, Y. N. Zhang and Q. L. Xu, *J. Nanosci. Nanotechnol.*, 2010, **10**, 5445; (c) S. Klosek and D. Raftery, *J. Phys. Chem. B*, 2001, **105**, 2815; (d) H. Yamashita, M. Harada, J. Misaka, M. Takeuchi, K. Ikeue and M. Anpo, *J. Photochem. Photobiol., A*, 2002, **148**, 257; (e) Y. Sakata, T. Yamamoto, T. Okazaki, H. Imamura and S. Tsuchiya, *Chem. Lett.*, 1998, 1253; (f) A. Fuerte, M. D. Hernández-Alonso, A. J. Maira, A. Martínez-Arias, M. Fernández-García, J. C. Conesa and J. Soria, *Chem. Commun.*, 2001, 2178.
- 4 A. L. Linsebigler, G. Lu and J. T. Yates Jr, *Chem. Rev.*, 1995, **95**, 735.
- 5 H. Tong, S. X. Ouyang, Y. P. Bi, N. Umezawa, M. Oshikiri and J. H. Ye, *Adv. Mater.*, 2012, **24**, 229.
- 6 A. Naldoni, M. D'Arienzo, M. Altomare, M. Marelli, R. Scotti, F. Morazzoni, E. Selli and V. Dal Santo, *Appl. Catal., B*, 2013, **130**, 239.
- 7 A. Naldoni, M. Allieta, S. Santangelo, M. Marelli, F. Fabbri, S. Cappelli, C. L. Bianchi, R. Psaro and V. Dal Santo, *J. Am. Chem. Soc.*, 2012, **134**, 7600.
- 8 H. M. Cao, Y. H. Zhu, X. Tan, H. G. Kang, X. L. Yang and C. Z. Li, *New J. Chem.*, 2010, **34**, 1116.
- 9 T. P. Cao, Y. J. Li, C. H. Wang, Z. Y. Zhang, M. Y. Zhang, C. L. Shao and Y. C. Liu, *J. Mater. Chem.*, 2011, **21**, 6922.
- 10 L. H. Tian, L. Q. Ye, J. Y. Liu and L. Zan, *Catal. Commun.*, 2012, **17**, 99.
- 11 (a) K. K. Akurati, A. Vital, J. P. Dellemann, K. Michalow, T. Graule, D. Ferri and A. Baiker, *Appl. Catal., B*, 2008, **79**, 53; (b) S. A. K. Leghari, S. Sajjad, F. Chen and J. L. Zhang, *Chem. Eng. J.*, 2011, **166**, 906; (c) A. K. L. Sajjad, S. Shamaila and J. L. Zhang, *J. Hazard. Mater.*, 2012, **235**, 307.
- 12 E. Formo, E. Lee, D. Campbell and Y. N. Xia, *Nano Lett.*, 2008, **8**, 668.
- 13 (a) N. X. Wang, C. H. Sun, Y. Zhao, S. Y. Zhou, P. Chen and L. Jiang, *J. Mater. Chem.*, 2008, **18**, 3909; (b) M. Shang, W. Z. Wang, L. Zhang, S. M. Sun, L. Wang and L. Zhou, *J. Phys. Chem. C*, 2009, **113**, 14727; (c) M. Shang, W. Z. Wang, W. Z. Yin, J. Ren, S. M. Sun and L. Zhang, *Chem.-Eur. J.*, 2010, **16**, 11412.
- 14 Z. Y. Liu, H. W. Bai and D. D. Sun, *Int. J. Photoenergy*, 2012, 804840.
- 15 L. Zhang, Y. G. Li, Q. H. Zhang and H. Z. Wang, *CrystEngComm*, 2013, **15**, 1607.
- 16 Q. H. Zhang, L. Gao and J. K. Guo, *Appl. Catal., B*, 2000, **26**, 207.
- 17 B. Yang, Y. J. Zhang, E. Drabarek, P. R. F. Barnes and V. Luca, *Chem. Mater.*, 2007, **19**, 5664.
- 18 X. L. Li, T. J. Lou, X. M. Sun and Y. D. Li, *Inorg. Chem.*, 2004, **43**, 5442.
- 19 G. C. Xi, B. Yue, J. Y. Cao and J. H. Ye, *Chem.-Eur. J.*, 2011, **17**, 5145.
- 20 C. H. Wang, C. L. Shao, X. T. Zhang and Y. C. Liu, *Inorg. Chem.*, 2009, **48**, 7261.
- 21 M. Penza, M. A. Tagliente, L. Mirengi, C. Gerardi, C. Martucci and G. Cassano, *Sens. Actuators, B*, 1998, **50**, 9.
- 22 Y. J. Liu and R. O. Claus, *J. Am. Chem. Soc.*, 1997, **119**, 5273.
- 23 C. F. Lin, C. H. Wu and Z. N. Onn, *J. Hazard. Mater.*, 2008, **154**, 1033.
- 24 K. S. W. Sing, *Pure Appl. Chem.*, 1982, **54**, 2201.
- 25 Z. H. Jiao, X. W. Sun, J. M. Wang, L. Ke and H. V. Demir, *J. Phys. D: Appl. Phys.*, 2010, **43**, 285501.
- 26 V. Keller, P. Bernhardt and F. Garin, *J. Catal.*, 2003, **215**, 129.
- 27 N. Zhang, S. Q. Liu, X. Z. Fu and Y. J. Xu, *J. Phys. Chem. C*, 2011, **115**, 9136.
- 28 (a) L. R. Zheng, Y. H. Zheng, C. Q. Chen, Y. Y. Zhan, X. Y. Lin, Q. Zheng, K. M. Wei and J. F. Zhu, *Inorg. Chem.*, 2009, **48**, 1819; (b) O. Legrini, E. Oliveros and A. M. Braun, *Chem. Rev.*, 1993, **93**, 671.
- 29 L. Jing, H. Fu, B. Wang, D. Wang, B. Xin, S. Li and J. Sun, *Appl. Catal., B*, 2006, **62**, 282.
- 30 (a) N. D. Abazović, M. I. Čomor, M. D. Dramićanin, D. J. Jovanović, S. P. Ahrenkiel and J. M. Nedeljković, *J. Phys. Chem. B*, 2006, **110**, 25366; (b) B. S. Liu, X. J. Zhao and L. P. Wen, *Mater. Sci. Eng., B*, 2006, **134**, 27.
- 31 C. Y. Su and H. C. Lin, *J. Phys. Chem. C*, 2009, **113**, 4042.
- 32 J. Ha, P. Muralidharan and D. K. Kim, *J. Alloys Compd.*, 2009, **475**, 446.